

Novel Approach for Assessing Cyclic Thermomechanical Behavior of Multilayered Structures

Benjamin Seligmann, Markus Alfreider, Michael Wurmshuber, and Daniel Kiener*

Microelectronic devices require material systems combining multiple layers of material for proper operation. These inevitably have different properties, for example, the elastic modulus or the coefficient of thermal expansion. Permanently reoccurring Joule heating and successive cooling during the operation of such devices lead to high thermal stresses within the materials and even failure due to thermomechanical fatigue or delamination of layers. This is dependent on the internal stress state and the amount of plastic strain accumulated. Here, in situ thermomechanical cantilever bending experiments on a Si–WTi–Cu material system to investigate these internal stress states and their influence on deformation behavior using a novel experimental methodology are shown. During heating to $T_{\max} = 400^{\circ}\text{C}$, the Cu layer undergoes partial plastic deformation, which may lead to the failure of a potential device using this material combination. To assess the internal stress and strain states based on the in situ observation, a model incorporating plastic deformation and known residual stresses of layers is proposed and verified by Finite Element Analysis.

1. Introduction

The technological progress in the microelectronics industry is ever-increasing. This influences many other fields as they depend on microelectronic devices, ranging from smartphones to car keys, from washing machines to space technology. As early as 1965, Gordon Moore predicted a doubling of transistors in a microchip every 2 years.^[1,2] 50 years later, this trend is still going on and leads to enormous numbers of transistors in ever-shrinking integrated circuits.

Thus, thermal management and the micromechanical properties of the used materials and their respective interfaces become a topic of major interest. As these microelectronic devices inevitably become repeatedly heated and cooled during their lifecycles, it is

very important to understand the thermo-mechanical fatigue mechanisms that may lead to the fatal failure of the device.^[3–5]


The presented work introduces a new micromechanical experimental setup, exploiting the known behavior of thermo-static bimetallic strips.^[6] When materials with different coefficients of thermal expansion α are combined, a temperature change will result in the bending of the material stack, implying mechanical stresses. Even though no physical contact, e.g., with an indenter is made, this kind of experimental setup is called “thermomechanical” throughout literature.^[7–10] Using a beam geometry and expanding on an elastic 2D model, the resulting stack curvature at the examined temperature enables to assess the internal stress and strain state of the respective layers.^[11]

The gathered information provides an understanding of maximum stress differences at interfaces as well as possible elastic–plastic responses of the material system, which, in the case of the presented experiments, is a well-known combination of Si, WTi, and Cu which is frequently used in microelectronic applications as substrate, diffusion barrier, and metallization layer, respectively.^[12–18]

Specific layers, interfaces, or the entire material stack have been investigated extensively in previous works. For example, Wimmer et al. studied the mechanical behavior of free-standing Cu films at different temperatures (refer to Sample A herein).^[19–22] It is also referred to those articles for more detailed information regarding microstructure, chemistry, and production of the material system. Bigl et al. investigated the thermomechanical high-cycle fatigue properties starting with the Cu film and extending their attention to the entire material system (also refer to Sample A therein).^[8,9,23,24] Furthermore, the WTi layer has been examined regarding its residual stresses and thermal stability.^[10,20,25] More recently, attention was placed on the properties of the interfaces, especially during fracture toughness experiments and cyclic heating.^[26–28] The present work expands this bulk of knowledge by assessing the actual occurring internal stresses during thermomechanical cycling.

These internal stresses and strains are essential for understanding the background of possible material damage during thermomechanical fatigue. These damages evidenced in high-cycle fatigue experiments include, for example, void and crack formation at interfaces that extend into the Cu layer,^[5,12,29,30] or roughening surfaces of the Cu layer due to diffusion processes

B. Seligmann, M. Alfreider, M. Wurmshuber, D. Kiener
Department Materials Science
Chair of Materials Physics
Montanuniversität Leoben
8700 Leoben, Austria
E-mail: daniel.kiener@unileoben.ac.at

 The ORCID identification number(s) for the author(s) of this article can be found under <https://doi.org/10.1002/adem.202201209>.

© 2022 The Authors. Advanced Engineering Materials published by Wiley-VCH GmbH. This is an open access article under the terms of the Creative Commons Attribution License, which permits use, distribution and reproduction in any medium, provided the original work is properly cited.

DOI: 10.1002/adem.202201209

and twin boundary migration.^[8] Thousands of short pulses using either an infrared furnace,^[12] ultrasonic resonance,^[29] or resistive heating of a polycrystalline Si layer^[30] were utilized for these experiments. Using only three cycles in the work herein presented, we want to understand the origins of the governing deformation mechanisms, which we presume lie in the internal stress-strain states.

The herein gathered insights provide complementary information to already established conventional methods, such as ion beam layer removal, X-ray diffraction, or wafer curvature measurements.^[6,31–38] Another advantage of the presented method is that the stress profile and other thermomechanical properties can be estimated, while one still benefits from the in situ nature of the experiment and the possibility of observing microstructural changes or the onset of potential damage formation.

2. Experimental Section

2.1. Material and Experimental Setup

The experiments were conducted on a layer stack synthesized on a (001)-oriented Si wafer. This stack was derived by first thermally growing an amorphous layer of SiO_x (50–70 nm), followed by a WTi layer of 250–300 nm deposited via physical vapor deposition. Using magnetron sputtering, a 300 nm Cu seed layer is utilized to subsequently deposit a 5 μm electrolytic Cu layer. Annealing at 400 °C for 30 min ensures a stable microstructure with a final grain size of 2.7 μm. This material stack was studied previously on separate occasions by Bigl et al.,^[8] Wimmer et al.,^[19] and Alfreider et al.,^[26] where further information regarding the growth of the multilayer stack and mechanical characterization can be found. A quantitative sketch of this multilayered material is depicted in **Figure 1a**. During the deposition process, the WTi layer experiences temperature changes, leading to compressive residual stresses of 1.5 GPa.^[10] Small pieces (around 3 × 10 mm) were broken from the wafer for sample preparation. Precutting of the cross-sectional area of the wafer

was performed on an Auriga platform (Carl Zeiss AG, Oberkochen, Germany) equipped with a femtosecond laser ablation unit (Origami 10 XP, Onefive GmbH, Regensburg, Switzerland),^[39] and focused ion beam (FIB) milling with currents ranging from 500 pA to 20 nA at a voltage of 30 kV was utilized to produce the final geometry (LEO 1540 XB, Carl Zeiss, Oberkochen, Germany). The high currents were used to establish rough cuts of the final sample geometry. These were reduced for the finer cuts and polishing steps to reduce the impact of Ga⁺ ion damage to the microstructure and prevalent residual stresses.^[40] This strategy was successfully implemented for similar sample dimensions in ion beam layer removal experiments, which suggests that no major changes in the initial residual stress state of the system are introduced.^[31,32] An example of a finished beam is shown in **Figure 1b**. The geometry of the samples was 95 to 100 μm in length, and the thickness of the Cu and Si layers was between 3.8 and 5.5 μm, equally distributed around the central WTi layer. In total four samples, with widths ranging from 3 to 9 μm were fabricated to study differences in deformation behavior.

The in situ experiments were conducted in a scanning electron microscope (SEM, DSM 982, Carl Zeiss AG, Oberkochen, Germany) using an apparatus capable of heating the sample holder via induction, the functionality of which is described in great detail elsewhere.^[41] After acclimatizing for about 48 h inside the SEM to ensure that organic surface contaminations are removed to a sufficient extent and that thermal equilibrium is reached, the samples were heated three times from room temperature (RT, air-conditioned 22 °C) to final temperatures, which were measured at the sample holder, between 275 and 400 °C. The offset to the actual sample temperature should not exceed 1 °C.^[41] These temperatures typically occur during the manufacturing of micro-electronic devices as well as during short circuits and represent the maximum temperature such devices should be able to endure.^[25] In regular temperature intervals, the temperature was held constant to take detailed images of the deflecting multilayer beam, with magnifications of 1000× and 5000× for curvature measurements, respectively. This leads to low heating rates with

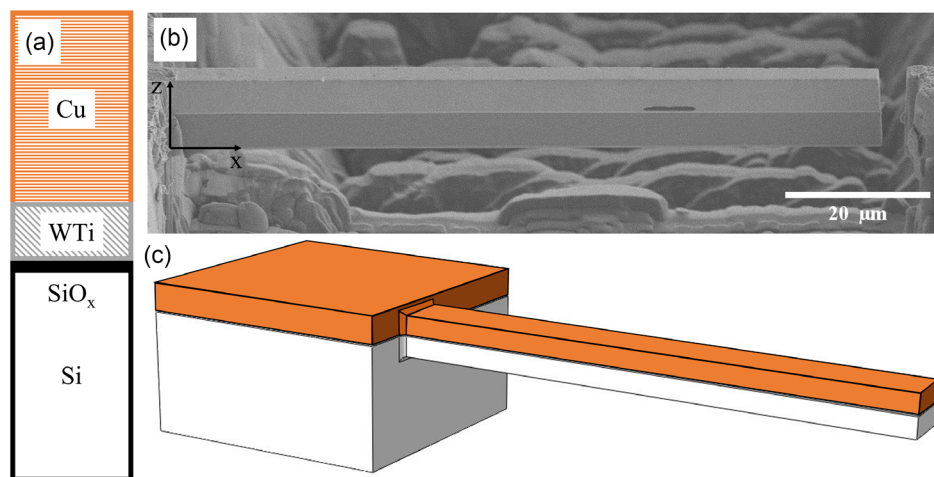


Figure 1. a) The studied material system is schematically shown in with the white Si substrate, the black SiO_x, the diagonally hatched, gray WTi, and the horizontally hatched, orange Cu layer. b) An example of the beam geometry is shown, c) while the used geometry for the finite element analysis (FEA) model is shown.

a maximum of $50\text{ }^{\circ}\text{C min}^{-1}$ between heating steps and approximately $4\text{ }^{\circ}\text{C min}^{-1}$ on average over the course of one heating cycle (an example heating cycle can be found in **Figure 2**). Between the individual cycles, the sample was cooled passively via thermal radiation and conduction through the sample holder which took approximately 60 min from $400\text{ }^{\circ}\text{C}$ back to RT.

2.2. Digital Image Correlation

To assess the curvature of the beam at the respective temperatures, the $5000\times$ detail images of the beam were stitched using paint.net (dotPDN LLC, Seattle, USA). The linear blending tool smoothed the overlapping areas. This leads to a panoramic image with a resolution of $30.8\text{ px }\mu\text{m}^{-1}$. In **Figure 1b** it is evident that the $\text{SiO}_x\text{-WTi}$ interface has the highest contrast. Therefore, this interface is chosen in further analysis to represent the curvature of the beam. To detect it, a semiautomatic pipeline was programmed in Python 3.8. This included a Canny edge detection algorithm, a masking step to reduce calculation time and memory usage, and conversion of the image to binary to apply a connecting composites algorithm.^[42] Several user inputs are required to optimize the detection of the interface. Used packages include OpenCV 4.0.1, NumPy 1.20.3, and SciPy 1.7.1. Using the bending line equation, it is physically reasonable to use a second-order polynomial equation to fit the individual perpendicular interface positions y of the beam as a function of temperature, as

$$z(x) = c_0 \frac{x^2}{2} + c_1 x + c_2 \quad (1)$$

The coordinates are represented by x in beam direction and z perpendicular to it, as shown in **Figure 1b**. Regarding this article, the beam is treated uniaxially due to its slender geometry as proposed by Timoshenko.^[43] Therefore, the curvature can be calculated considering the second derivative of the x - y relationship in Equation (1) as

$$\kappa = -\frac{d^2 z}{dx^2} = -2c_0 \quad (2)$$

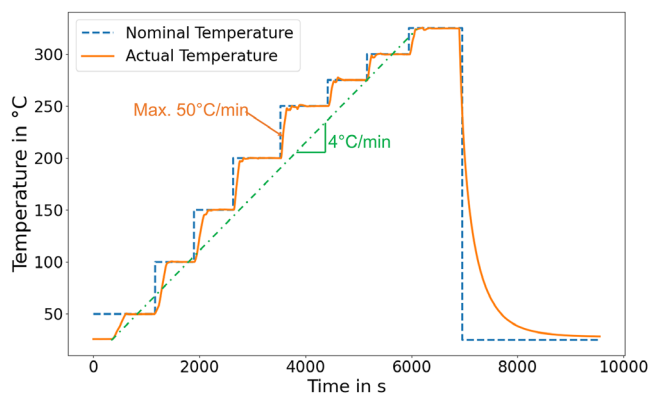


Figure 2. A typical heating cycle, showing the nominal (blue, dashed line) and the actual temperature (orange, solid line) as well as the average heating rate (green, dash dotted) and the maximum heating rates between scanning electron microscope (SEM) image taking.

Using the determined curvature values and their corresponding temperatures allows for useful insights into internal stress states, as will be explained later.

2.3. Finite Element Analysis

To validate the experimental results, FEA was conducted using ABAQUS (Dassault Systèmes SE, France). Similar simulations showed that it is necessary to model a portion of the bulk wafer the beam is attached to.^[31] **Figure 1c** shows the chosen geometry. The bulk part was $50 \times 50 \times 50\text{ }\mu\text{m}^3$, while the exact beam geometry was taken from the respective samples. The rounding of the edges was chosen by educated estimates. The offset of the front edge of the wafer is $10\text{ }\mu\text{m}$. For the Si and WTi layer, linear elastic behavior is assumed, while the Cu layer was modeled with a perfectly plastic onset after the elastic regime (this is called yield strength and will be denoted as σ_y). This onset is temperature-dependent and was investigated in prior works by Wimmer et al.^[22]

The used material parameters are listed in **Table 1**. Regarding the meshing, hexagonal linear elements were used and the maximum element size was at most a fifth of the respective layer thickness. The earlier mentioned compressive stresses were also implemented as a biaxial stress state in the WTi layer. The chosen boundary conditions on the bulk part of the model restricted the translational movement of the three sides not visible in **Figure 1c** in the normal direction of the respective plane.

2.4. Internal Stress Model

To estimate the internal stresses, a model was built on a bilayer approach proposed by Chu.^[11] It can be seen in **Figure 3a** how a material stack behaves during heating in the case that $\alpha_1 < \alpha_2$, α being the coefficient of thermal expansion. Due to the larger α_2 , the upper layer expanded more than the lower layer, resulting in the curvature of the beam and a stress discontinuity. The strain on the other hand experienced a continuous behavior as long as no delamination occurs (compare **Figure 3b** for the elastic case of three layers). Chu's model is solved only for elastic material responses and did not consider additional layers or residual stresses. Therefore, these important points shall be addressed

Table 1. Used mechanical properties for the FEA model, including young's modulus E , and Poisson's ratio ν .

Material	E [GPa]	ν [-]	α [$\text{Wm}^{-1}\text{K}^{-1}\cdot 10^{-6}$]	T [$^{\circ}\text{C}$]	σ_y [MPa]
Si	170 ^[52]	0.25 ^{a)}	2.6 ^[6]	—	—
WTi	330 ^[53]	0.34 ^[54]	4.5 ^[55]	—	—
Cu	110 ^[56]	0.35 ^[57]	16.7 ^[6]	20 ^[22]	142 ^[22]
				100 ^[22]	140 ^[22]
				125 ^[22]	130 ^[22]
				150 ^[22]	125 ^[22]
				200 ^[22]	107 ^[22]
				400 ^[22]	79 ^[22]

^{a)}Average from multiple sources.^[52,58,59]

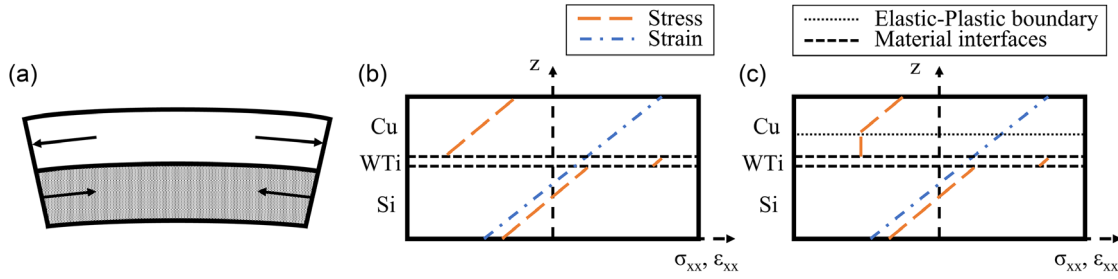


Figure 3. Illustration of the heating of two layers of materials with different coefficients of: a) thermal expansion. b) Qualitative sketch of the elastic and c) plastic case of the proposed PARS model.

in the derivation of the present improved model, which we shall name PARS standing for plastic and residual stresses.

2.4.1. Elastic Case

The stresses within the three layers can be calculated using the following equations

$$\sigma_{xx, Si}(z) = E_{Si} \left[\left(z - \frac{t_{Si}}{2} \right) \kappa + \epsilon_{Si} \right] \quad (3.1)$$

$$\sigma_{xx, WTi}(z) = E_{WTi} \left[\left(z - \left(t_{Si} + \frac{t_{WTi}}{2} \right) \right) \kappa + \epsilon_{WTi} \right] + \sigma_{WTi} \quad (3.2)$$

$$\sigma_{xx, Cu}(z) = E_{Cu} \left[\left(z - \left(t_{Si} + t_{WTi} + \frac{t_{Cu}}{2} \right) \right) \kappa + \epsilon_{Cu} \right] \quad (3.3)$$

The normal stresses in x -direction σ_{xx} are in dependence of z , the variable in stacking direction. The thicknesses of the individual layers are denoted by t_i and ϵ_i is the uniaxial strain acting on the respective layer. The residual stresses of the WTi layer are added by σ_{WTi} . If residual stresses of other layers are known, these can be implemented likewise. As no delamination occurs between the layers, the continuous strain leads to the following invariant points at the respective interfaces

$$\epsilon_{xx, Si}(z = t_{Si}) = \epsilon_{xx, WTi}(z = t_{Si}) \quad (4.1)$$

$$\epsilon_{xx, WTi}(z = t_{Si} + t_{WTi}) = \epsilon_{xx, Cu}(z = t_{Si} + t_{WTi}) \quad (4.2)$$

with

$$\epsilon_{xx, Si}(z) = \left(z - \frac{t_{Si}}{2} \right) \kappa + \epsilon_{Si} + \alpha_{Si} \Delta T \quad (5.1)$$

$$\epsilon_{xx, WTi}(z) = \left(z - \left(t_{Si} + \frac{t_{WTi}}{2} \right) \right) \kappa + \epsilon_{WTi} + \alpha_{WTi} \Delta T \quad (5.2)$$

$$\epsilon_{xx, Cu}(z) = \left(z - \left(t_{Si} + t_{WTi} + \frac{t_{Cu}}{2} \right) \right) \kappa + \epsilon_{Cu} + \alpha_{Cu} \Delta T \quad (5.3)$$

The resulting equilibrium of forces within the beam can be expressed as

$$\Sigma F = 0 = E_{Si} t_{Si} \epsilon_{Si} + E_{WTi} t_{WTi} \epsilon_{WTi} + E_{Cu} t_{Cu} \epsilon_{Cu} + \sigma_{WTi} t_{WTi} \quad (6)$$

Solving Equation (3)–(6) leads to an analytical solution to the problem in the elastic case.

2.4.2. Plastic Case

In the case of the plastification of one of the layers, the model becomes more intricate. As WTi and Si both remain elastic within the conducted experimental settings, only Cu is considered to deform plastically. This case is schematically shown in Figure 3c. At high temperatures, the compressive stresses exceed the yield strength and plastic deformation initiates at the WTi–Cu interface. Increasing the temperature further deforms a larger volume of material plastically. The plasticity shall be estimated with a bilinear hardening model (Figure 4a). This is possible as the required ultimate tensile strength data and the corresponding strains are available at different temperatures between RT and 400 °C.^[22] Combined with the data regarding the yield strength σ_y , it is possible to estimate a linear hardening modulus H . This leads to a behavior sketched in Figure 3c and the splitting of the Cu layer into two parts, refining Equation (3.3) to

$$\sigma_{xx, Cu}(z) = \begin{cases} H_{Cu} \left[\left(z - \left(t_{Si} + t_{WTi} + \frac{t_{Cu}}{2} \right) \right) \kappa + \epsilon_{Cu} \right] + \sigma_{y, Cu} + \sigma_h, & \sigma_{xx, Cu} > \sigma_{y, Cu} + \sigma_h \\ E_{Cu} \left[\left(z - \left(t_{Si} + t_{WTi} + \frac{t_{Cu}}{2} \right) \right) \kappa + \epsilon_{Cu} \right] + \sigma_h, & \sigma_{xx, Cu} \leq \sigma_{y, Cu} + \sigma_h \end{cases} \quad (7)$$

Due to the plastic deformation upon annealing (loading), tensional residual stresses are induced after cooling to RT (unloading), which are accounted by σ_h .

These internal stresses can be calculated using the bilinear hardening model at different temperatures in hysteresis of

compression and tension (compare Figure 4b). The dotted red line shows the actual behavior, while the green line shows the simplified behavior which is sufficient for calculations. Starting at any residual stress value $\sigma_{h,i}$ the sample is heated from RT and deforms elastically. As the yield strength decreases with

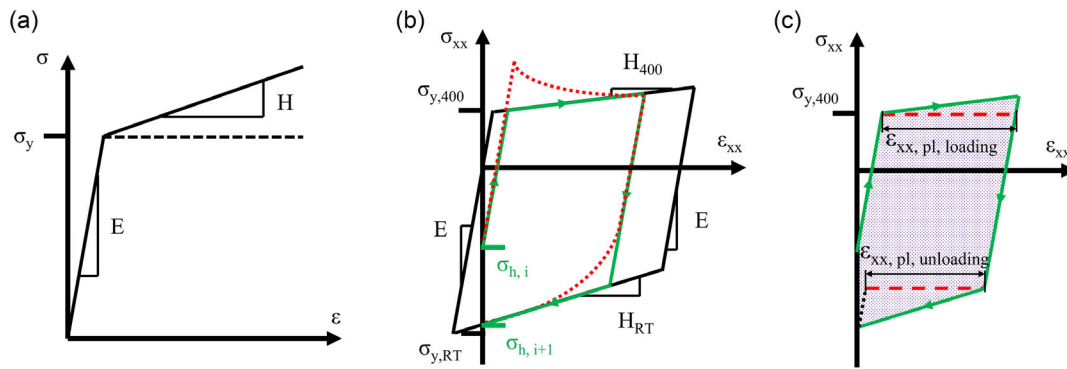


Figure 4. a) Depiction of the Cu deformation state for a bilinear hardening model. b) During plastic deformation, residual stresses σ_h are induced in the copper layer. This process is shown by the red, dotted line (actual behavior) and the green line (approximation used for calculations). c) The dissipated energy during a heating cycle is shown by the shaded area and the plastic strain is depicted by the dashed red lines.

increasing temperature the trend of the red line is observed, where after a first initial yield at some temperature, the stress decreases since the yield limit decreases as well with further increasing temperature. After fully heating to 400 °C, the green and red line join in the same stress–strain value pair. This is true for any final temperature, which is the reason why the approximation of the green line is valid. It should be pointed out that this decrease in stress is not related to stress relaxation, but only to the decrease in yield strength with increasing temperature, as a stable microstructure can be expected up to 400 °C in the Cu layer, ensured by a prior heat treatment at 400 °C after multilayer stack fabrication.^[8] Upon cooling the beam deforms elastically up to a yield point corresponding to that temperature. Now, the temperature decreases further, which increases the yield strength. Therefore, the green line approximation is again valid, as at RT both lines coincide again. This point arises from the yield strength and the plastic modulus H_{RT} at RT.

This combination of elastic–plastic properties at elevated and RT gives rise to a hysteresis, which allows calculating the residual stresses within the plastically deformed copper layer, but also the plastic strain and the dissipated energy due to deformation (see Figure 4c).

To complete the set of equations necessary for solving the plastic case, the equilibrium of forces can be written as follows. Note that it changes considerably to the elastic version in Equation (6), as several new terms are added.

$$\begin{aligned} \Sigma F &= 0 \\ &= E_{Si}t_{Si}\epsilon_{Si} + E_{WTi}t_{WTi}\epsilon_{WTi} + t_{Cu}\epsilon_{Cu}(xH_{Cu} + (1-x)E_{Cu}) \\ &\quad + \sigma_{WTi}t_{WTi} + \sigma_{y,Cu}t_{Cu} + \sigma_h t_{Cu} \end{aligned} \quad (8)$$

The ratio between elastic and plastic deformation is denoted by x (compare Figure 3c and Equation (7)). The resulting system of Equations (3.1), (3.2), (4.1), (4.2), (7), and (8) is only solvable numerically, which is done using Newton's method to obtain the root of the homogeneous force equilibrium equation.

It shall be pointed out that this approach can be easily extended to more layers, resulting in more but similar equations.

3. Results

The measured curvature values with their corresponding temperatures can be found in Figure 5. As the general trends are the same for all samples, the green sample in Figure 5 is chosen for representation purposes. A representative heating cycle is depicted in Figure 2 showing the heating of the sample in steps to take SEM images (as can be seen in Figure 6), followed by passive cooling. An actual video of the experiment can be found online in Supporting Information S1.

Analyzing the curvature and temperature values via the equation system proposed in the preceding chapter yields the results shown in Figure 7. Using the FEA model, the same information can be extracted. This is done by measuring the internal stress vertically at the geometric center of the beam. The resulting graphs are shown in Figure 8. In both figures, the horizontal axis depicts the stresses and strains within the beam, while the vertical axis shows the material stack using the corresponding color scheme to Figure 1a. The left column shows the stress conditions within

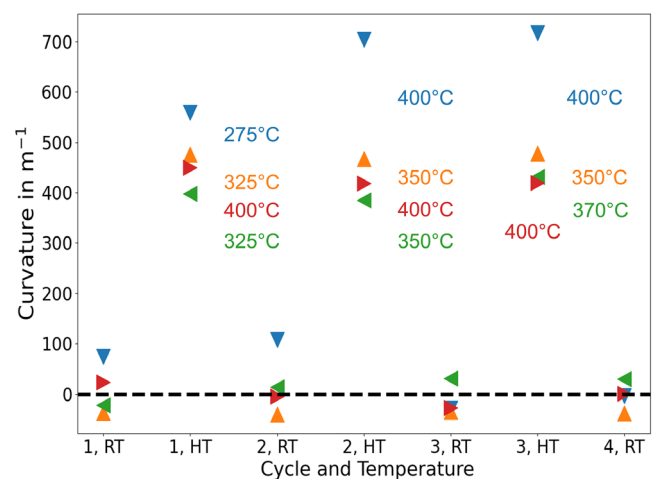


Figure 5. Curvature values as a function of three consecutive heating cycles. RT stands for room temperature; HT refers to high temperature. The specifically reached peak values are written in the corresponding color next to the symbols.

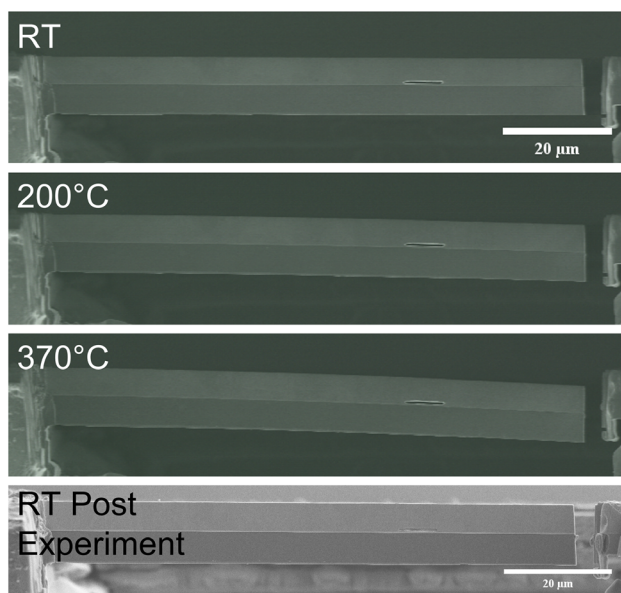


Figure 6. Three steps of the heating cycle, starting at RT, followed by 200 and 370 °C. With increasing temperature, the curvature value increases as well. The last image shows the final state after cycling.

the multilayer stack at RT, while the right column shows the high-temperature configuration, with the exact temperature labeled at the top of the graph. Each row depicts one heating cycle. In Figure 7a, 8a the elastic deformation due to the residual stresses in the WTi layer can be observed, as the stresses deviate from zero. Starting with Figure 7b, 8b dash-dotted lines are introduced to indicate boundaries between elastic and plastic deforming regions. Below this line, the Cu layer is plastically deformed as the stress exceeds the yield strength at this temperature. Also, the elastic region of the Cu layer as well as the Si and WTi layer show a typical elastic stress gradient. The residual stresses within the WTi layer are distributed onto the Cu and Si layer. In the following RT plots, starting with Figure 7c, 8c, two dash-dotted lines are shown. The upper one corresponds to the elastic–plastic border, similar to the preceding one, while the lower one indicates the boundary between the material that has been solely plastically deformed at high temperatures and the material beneath it, which has been plastically deformed during heating as well as cooling steps. This results due to reverse bending, which introduces tensile stresses that exceed the yield strength at RT. The next Figure 7d, 8d illustrates the fact that higher temperatures deform a larger volume plastically compared to Figure 7b, 8b ($\Delta T = 25^\circ\text{C}$). Up to Figure 7g, 8g, the following heating cycles are shown, with similar trends as described up to this point. Figure 7h, 8h summarizes the total plastic strain after all heating cycles at the end of the experiment. In this figure, it is evident that at the interface between WTi and Cu the highest strains are accumulated, as the highest stresses are repeatedly introduced there.

4. Discussion

In the following, it shall be discussed to what extent the proposed PARS model is suited to estimate the internal stresses in

thermomechanical, cyclic experiments compared to the FEA simulation. At the beginning of the experiment, the FEA model starts with an initial curvature value of $\kappa = 0\ \mu\text{m}^{-1}$, as no optimizing algorithm was implemented into the FEA model. This is only true as long as no residual stresses in any layer are considered. As this is clearly not the case considering the experimental data, the starting point is more accurately predicted by the proposed analytical model, as it considers the initial curvature of the beam. It therefore always fulfills the condition $\Sigma F = 0$.

After the initial heating step, the differences between the two models become less significant. The curving of the beam leads to increasing stress gradients in all layers, which is resembled in the plots of Figure 7 and 8 by a decreasing slope, as it is inverse proportional to the stress gradient. The residual stresses within the WTi layer relax significantly, while the Si layer shifts into the tensile stress regime. As a bilinear stress–strain relationship is used for the approximation of hardening in the proposed model, the border between elastic and plastic deformation within the Cu layer is quite distinct. Following a similar trend, the FEA model shows a smoother transition from elastic to plastic deformation toward the WTi–Cu interface. Later cycles experience higher temperatures, which leads to a larger plastically deformed portion of the Cu layer.

Figure 9a compares both models at the final state of experiment. As discussed earlier, the stress behavior is similar in both cases, showing small or even negative stress values at the top of the film, slowly changing to tensile stresses close to the yield strength at RT. However, one difference is the behavior close to the WTi–Cu interface. The PARS model shows a decrease in stress level, which can be related to the remaining curvature at this temperature (RT). Therefore, an advantage of the PARS model can be highlighted as it considers actual experimental values, showing that maximum tensile stress is experienced not directly at the interface, but, depending on the curvature, at or above the interface, whereas the FEA model does not use this information. This remaining curvature can be linked to the already-mentioned residual stresses in the individual layers.

Comparing the two plots showing the accumulated plastic strain reveals the same characteristics (Figure 9b). A small portion at the top of the beam of $\approx 1\ \mu\text{m}$ in height is only elastically deformed. The FEA model predicts less strain at the top of the layer and a larger absolute value for the accumulated strain at the interface, but both models produce values in the same order of magnitude. Further experiments with different beam widths indicate that the discrepancy between the models increases with beam width, as can be seen in Figure 9c, but trends and order of magnitude stay the same. The proposed PARS model does not account for the width of the beam, while the 3D model of the FEA analysis does. The discrepancy is expected as the geometry of thin film structures has a considerable influence on the yield stress of the material.^[44,45] Usually, this is linked to film thickness, but it may be extended to the width of the sample beam. Still, it should be pointed out that the general trends can be modeled quite well even for thicker beams and only the quantitative results differ slightly. The models differ in their implementation of plastification. The FEA model uses a perfectly plastic yield, while the PARS model used a bilinear hardening approach. As the Cu layer shows homogeneous deformation in the plastic regime this approach is sufficient, since it makes both models as

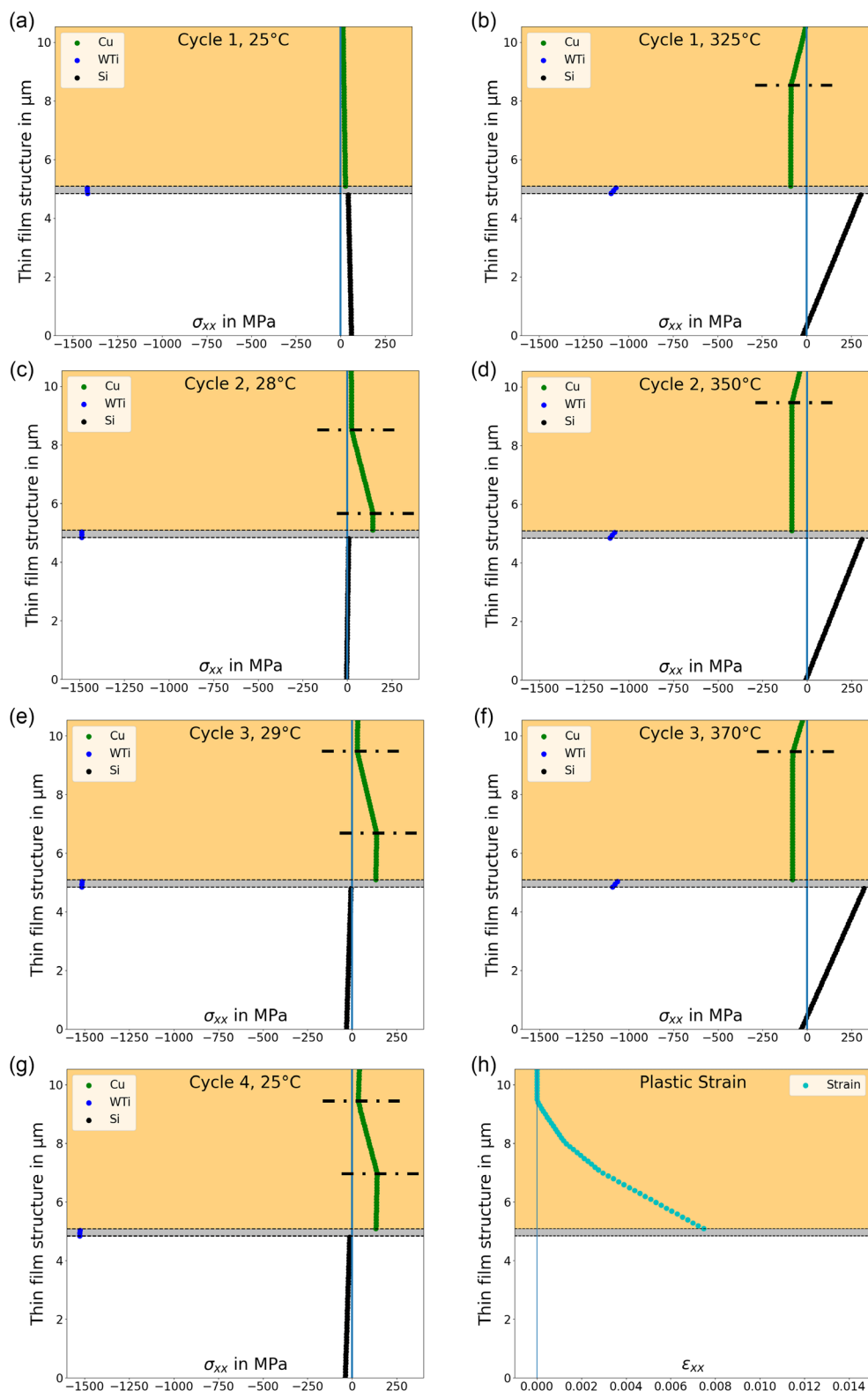


Figure 7. a–g) Stress and h) total plastic strain accumulated after thermal cycling plots produced by experimental data and the PARS model. Every row shows a cycle where the left column depicts the stresses at RT, while the right column depicts the situation at maximum cycle temperature. The dash dotted lines divide the Cu layer into regions of elastic deformation (top), plastic deformation during heating (middle), and plastic deformation during heating and cooling (bottom) in the left column. For the right column, it divides the Cu layer into the elastic (top) and plastic (bottom) parts.

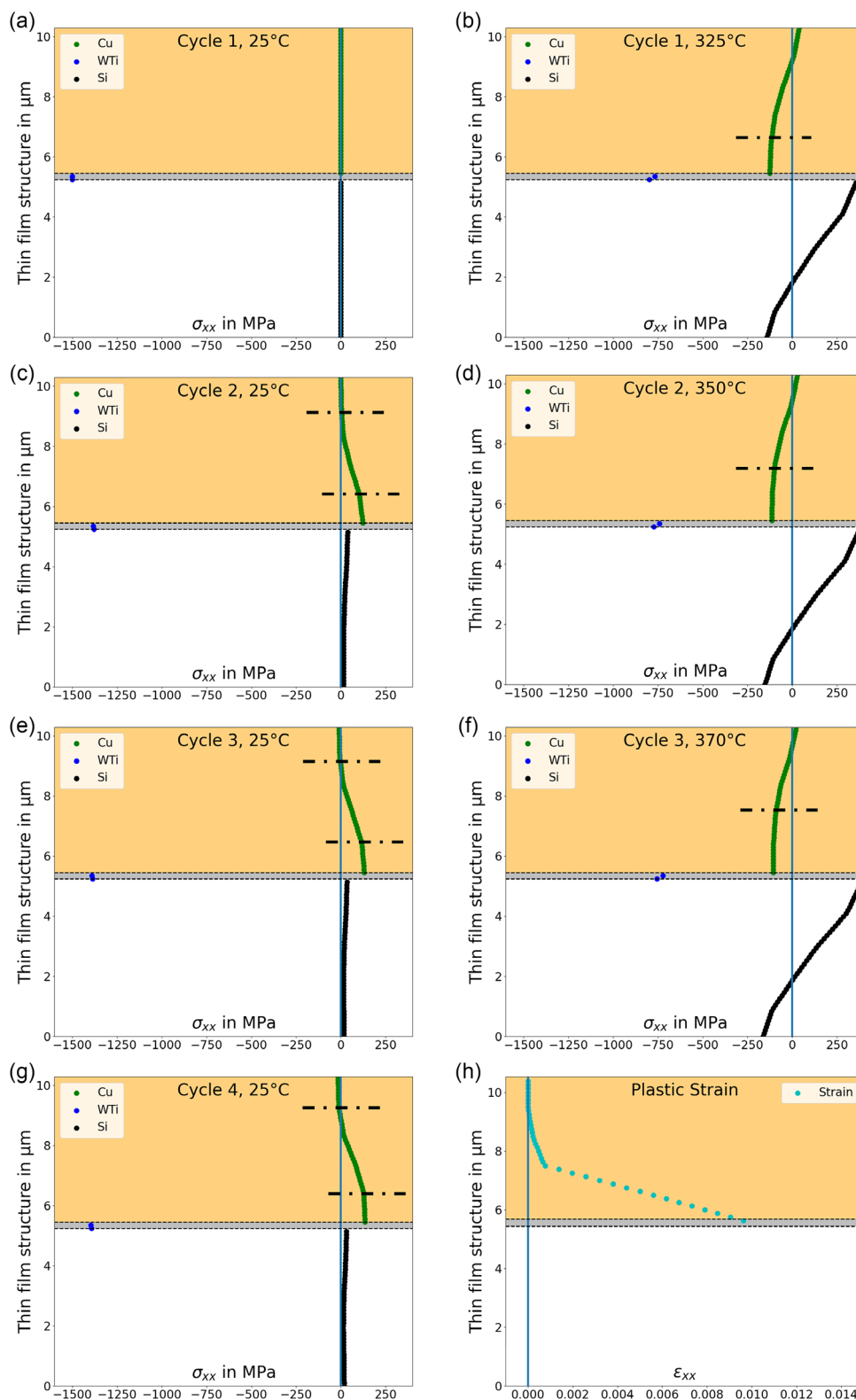


Figure 8. a–g) Stress and h) total plastic strain accumulated after thermal cycling plots produced by the FEA model. Every row shows a cycle where the left column depicts the stresses at RT, while the right column depicts the situation at maximum cycle temperature. The dash dotted lines divide the Cu layer into regions of elastic deformation (top), plastic deformation during heating (middle), and plastic deformation during heating and cooling (bottom) in the left column. For the right column, it divides the Cu layer into the elastic (top) and plastic (bottom) parts.

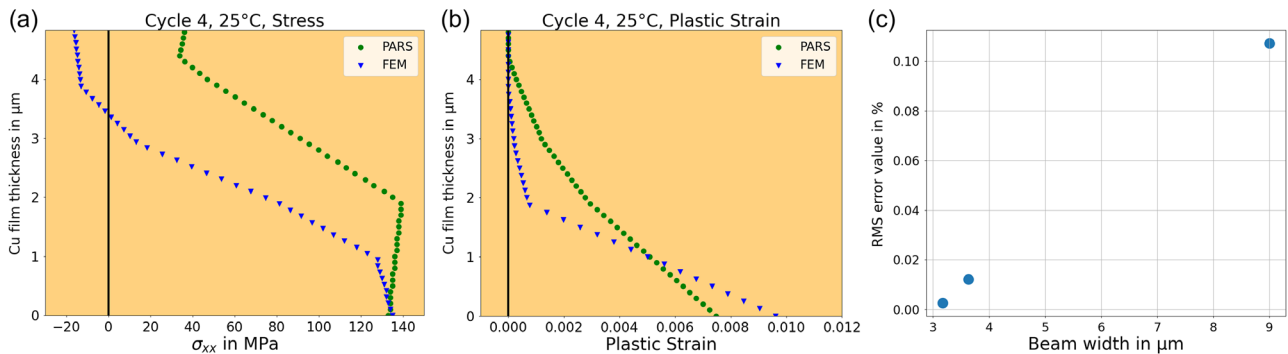


Figure 9. Comparison of the final state after the experiment, in terms of: a) stress- and b) strain-distribution. In c) the root mean squared (RMS) difference between PARS and FEA model is shown versus the beam width.

streamline as possible. If one were to use temperature-dependent σ - ϵ curves, this would imply a lot of background interpolation between the temperatures.

The plastic modulus never gets higher than $H = 3 \text{ GPa}$.^[22] However, this is data which is derived from tensile experiments. As was explained in Figure 4b, 7, and 8, parts of the Cu layer get deformed plastically in tension and compression. For the first step, it is adequate to use only tensional data as this is the conservative approach. But the compressional flow curve differs from the tensional one, which suggests a possibility to improve the models.^[46] The data for this specific Cu layer was not available during experimental evaluation, but it is indicated by RT nanoindentation experiments that the yield strength is approximately twice as high in compression than in tension.^[9,46]

If available, the PARS model could be extended to use hardening behavior information of the respective materials from flow curves determined in tension and/or in compression. However, the main point of this work is to show a proof of concept of a simple analytical model. Therefore, the implementation of more complex models will remain the focus of future work.

During the heating cycles, high temperatures of up to 400°C are reached. Especially in Cu, this might lead to significant relaxation processes or even microstructural changes as this temperature is equivalent to 50% of the melting point of pure Cu.^[47] In the present case, however, a stable microstructure is ensured due to a heat treatment of the material stack after fabrication at 400°C for 30 min. Therefore, no relaxation is expected to take place during heating to temperatures of 400°C and below, especially as holding times at higher temperatures never exceeded 10 min.

Both models consider the residual stresses in the Cu and Si layers to be zero. This assumption is not entirely true, as during

deposition the residual stresses of WTi have to be countered by the Si wafer. It was shown that these are not distributed evenly by ion beam layer removal experiments.^[32,48] Nevertheless, it shall be assumed that residual stresses are spread evenly within each layer as a first-order approximation to simplify the mathematical models. A 250 nm thick WTi layer with -1.5 GPa compressive stress induces 0.5 MPa in a 725 μm thick Si wafer. This justifies the assumption of a quasi-stress-free substrate, which is also encouraged by findings produced with the ion beam layer removal method.^[31,48,49]

In the ion beam layer removal experiments conducted by Chen et al., the residual stresses found in a 400 nm Cu layer were as high as 200 MPa.^[48] Considering that the yield strength and the ultimate tensile strength of the herein-used Cu are smaller than 200 MPa, this estimate shall suffice for the purpose of illustration. In a 5 μm layer of Cu, this would lead to 16 MPa, which equals around 10% of the yield strength of the material. This might not have a significant impact on the predictions of the models, but still should be considered for future experiments. Notably, with the herein-presented experimental setup, it is not possible to measure the residual stresses of the individual layers. Therefore, an alternative experimental setup shall be proposed, which in combination with the introduced model is capable of calculating the residual stresses within a three-layer material stack.

Again, it is assumed that the substrate is free of stresses. Therefore, $\sigma_{\text{Si}} = \sigma_{\text{r,Si}} = 0 \text{ MPa}$ is known. $\sigma_{\text{r,Si}}$ depicts the residual stress of the Si layer. In Figure 10, one can see the proposed setup for the experiment. During sample preparation, another beam is prepared with the same geometry and a removed Cu layer. The resulting curvature is solely related to the residual

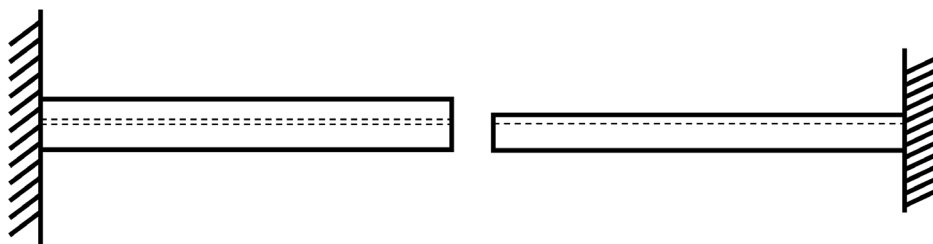


Figure 10. Suggested experimental setup for a concurrent bi- and trilayer experiment.

stresses within the WTi layer. For the bilayer, the equation system introduced in Section 2.4.1 is simplified and reduces to Equation (3.1), (3.2), (4.1), (5.1), and (5.2). The force equilibrium is then expressed as

$$\Sigma F = 0 = E_{Si}t_{Si}\epsilon_{Si} + t_{WTi}(E_{WTi}\epsilon_{WTi} + \sigma_{r,WTi}) \quad (9)$$

$\sigma_{r,WTi}$ can thus be determined iteratively, for example, using Newton's method. However, it is important to stay in the elastic regime of the material combination.

Using $\sigma_{r,WTi}$ leads to the elastic case depicted in Section 2.4.1 with Equation (3.3) and (6) changing to

$$\sigma_{xx,Cu}(z) = E_{Cu} \left[\left(z - \left(t_{Si} + t_{WTi} + \frac{t_{Cu}}{2} \right) \right) \kappa + \epsilon_{Cu} \right] + \sigma_{r,Cu} \quad (10)$$

$$\Sigma F = 0$$

$$= E_{Si}t_{Si}\epsilon_{Si} + t_{WTi}(E_{WTi}\epsilon_{WTi} + \sigma_{r,WTi}) + t_{Cu}(E_{Cu}\epsilon_{Cu} + \sigma_{r,Cu}) \quad (11)$$

Again, $\sigma_{r,Cu}$ has to be determined by iteration and it should be noted that plastic deformation is not considered by this model. Therefore, the curvature should be measured at RT and small elevated temperatures (50 °C). Subsequently, the gathered residual stresses can be implemented into the plastic case as performed in this article for the WTi layer.

In this work, residual stresses are treated to be constant over the layer thickness. While this simplified assumption delivers reasonable quantitative results, it could be improved by experimentally obtained residual stress gradients determined, for example, by ion beam layer removal or the ring hole and core milling methods.^[31,32,37,38,48–51] However, this would be a significant work in its own right and therefore not covered within this article.

This setup is closely related to the ion beam layer removal method and other residual stress measurements techniques like X-ray diffraction or wafer curvature measurements.^[6,31–38] The advantage of the present method is that residual stresses can be estimated in the same experiment as thermomechanical properties, while still being an in situ experiment capable of observing microstructural changes and the potential onset of damage formation.

5. Conclusion

The goal of the proposed experimental setup and model was to provide a simple tool to estimate the internal stresses of multi-layered structures during thermomechanical cycling. In general, an existing model was extended to three-layer systems, including residual stresses of layers and enabling plastic deformation within the layers. Based on experimental microscale curvature data, the generated results were compared to a 3D FEA model. Internal stress distribution trends and the accumulated strain agree well in both models, suggesting the proposed model to be sufficient for fast estimates or large-scale screening purposes. Furthermore, this can be useful when assessing the stress difference at layer interfaces, which could be linked to the delamination of these layers.^[28] As the model does only consider two dimensions, the agreement of both models gets increasingly further with increasing sample width but stays within reasonable

limits. However, it is quite evident that the amount of time saved is significant. As the FEA model is 3D, the simulations took time spans in the order of 10 to 20 min for every sample, while the PARS model calculates and saves plots within seconds for all samples.

With the used experimental setup, it is not possible to independently measure the residual stresses of the respective layers. Therefore, a new experimental strategy is proposed that enables simultaneous measurement of residual stresses and the assessment of cyclic thermomechanical behavior. The analytical model and the adapted experimental setup are applicable to other material structures as well and could be conveniently employed for systems with more than three layers, too, thus accounting for the common complexity in modern microelectronic systems. If necessary, more complex hardening models of plastic layers as well as more detailed residual stress profiles within the layers could be incorporated if the respective information were available for the respective system.

Supporting Information

Supporting Information is available from the Wiley Online Library or from the author.

Acknowledgements

The authors gratefully acknowledge the financial support under the scope of the COMET program within the K2 Center "Integrated Computational Material, Process and Product Engineering, IC-MPPE" (Projects A2.22). This program is supported by the Austrian Federal Ministries for Transport, Innovation and Technology (BMVIT) and for Digital and Economic Affairs (BMDW), represented by the Österreichische Forschungsförderungsgesellschaft (Funder ID: 10.13039/50110 0 0 04955), and the federal states of Styria, Upper Austria, and Tyrol. This project has received funding from the European Research Council (ERC) under the European Union's Horizon 2020 research and innovation programme (Grant No. 771146 TOUGHIT).

Conflict of Interest

The authors declare no conflict of interest.

Data Availability Statement

The data that support the findings of this study are available from the corresponding author upon reasonable request.

Keywords

copper, finite element modeling, stress modeling, thermomechanical fatigue, thin films

Received: August 23, 2022

Revised: November 14, 2022

Published online: December 7, 2022

[1] G. E. Moore, *Electronics* **1965**, 38, 114.

[2] G. E. Moore, presented at *International Electron Devices Meeting*, Washington DC, December **1975**.

- [3] R. R. Keller, R. Mönig, C. A. Volkert, E. Arzt, R. Schwaiger, O. Kraft, presented at *AIP Conf. Proceedings of the 6th Inter. Workshop of Stress Induced Phenomena in Metallization*, Vol. 612, AIP, Melville, NY, **2002**, pp. 119–132.
- [4] W. D. Nix, *Metall. Mater. Trans. A* **1989**, 20, 2217.
- [5] M. Nelhiebel, R. Illing, C. Schreiber, S. Wöhlert, S. Lazerstorfer, M. Ladurner, C. Kadow, S. Decker, D. Dibra, H. Unterwalcher, M. Rogalli, W. Robl, T. Herzig, M. Poschgan, M. Inselsbacher, M. Glavanovics, S. Fraissé, *Microelectron. Reliab.* **2011**, 51, 1927.
- [6] L. B. Freund, S. Suresh, *Thin Film Materials: Stress, Defect Formation and Surface Evolution*, Cambridge University Press, Cambridge, UK **2004**.
- [7] D. Weiss, H. Gao, E. Arzt, *Acta Mater.* **2001**, 49, 2395.
- [8] S. Bigl, S. Wurster, M. J. Cordill, D. Kiener, *Materials* **2017**, 10, 1287.
- [9] S. Bigl, S. Wurster, M. J. Cordill, D. Kiener, *Thin Solid Films* **2016**, 612, 153.
- [10] S. Wurster, S. Bigl, M. J. Cordill, D. Kiener, *Microelectron. Eng.* **2017**, 167, 110.
- [11] S. N. G. Chu, *J. Electrochem. Soc.* **1998**, 145, 3621.
- [12] G. Kravchenko, B. Karunamurthy, M. Nelhiebel, H. E. Pettermann, presented at the *2013 EuroSimE*, Wroclaw, Poland **2013**.
- [13] J. O. Olowolafe, C. J. Mogab, R. B. Gregory, *Thin Solid Films* **1993**, 227, 37.
- [14] M. Fugger, M. Plappert, C. Schäffer, P. Humbel, H. Hutter, H. Danninger, M. Nowotnick, *Microelectron. Reliab.* **2014**, 54, 2487.
- [15] J. L. Liotard, D. Gupta, P. A. Psaras, P. S. Ho, *J. Appl. Phys.* **1985**, 57, 1895.
- [16] C. Kalha, S. Bichelmaier, N. K. Fernando, J. V. Berens, P. K. Thakur, T.-L. Lee, J. J. Gutiérrez Moreno, S. Mohr, L. E. Ratcliff, M. Reisinger, J. Zechner, M. Nelhiebel, A. Regoutz, *J. Appl. Phys.* **2021**, 129, 195302.
- [17] R. Rosenberg, D. C. Edelstein, C. K. Hu, K. P. Rodbell, *Ann. Rev. Mater. Sci.* **2000**, 30, 229.
- [18] J. C. Anderson, *Thin Solid Films* **1972**, 12, 1.
- [19] A. Wimmer, M. Smolka, W. Heinz, T. Detzel, W. Robl, C. Motz, V. Eyert, E. Wimmer, F. Jahnel, R. Treichler, G. Dehm, *Mater. Sci. Eng.* **2014**, 618, 398.
- [20] A. Wimmer, A. Leitner, T. Detzel, W. Robl, W. Heinz, R. Pippan, G. Dehm, *Acta Mater.* **2014**, 67, 297.
- [21] A. Wimmer, W. Heinz, T. Detzel, W. Robl, M. Nellessen, C. Kirchlechner, G. Dehm, *Acta Mater.* **2015**, 83, 460.
- [22] A. Wimmer, W. Heinz, A. Leitner, T. Detzel, W. Robl, C. Kirchlechner, G. Dehm, *Acta Mater.* **2015**, 92, 243.
- [23] S. Bigl, T. Schöberl, S. Wurster, M. J. Cordill, D. Kiener, *Surf. Coat. Technol.* **2016**, 308, 404.
- [24] A. Kleinbichler, J. Todt, J. Zechner, S. Wöhlert, D. M. Többsen, M. J. Cordill, *Surf. Coat. Technol.* **2017**, 332, 376.
- [25] C. Kalha, M. Reisinger, P. K. Thakur, T.-L. Lee, S. Venkatesan, M. Isaacs, R. G. Palgrave, J. Zechner, M. Nelhiebel, A. Regoutz, *J. Appl. Phys.* **2022**, 131, 165301.
- [26] M. Alfreider, J. Zechner, D. Kiener, *JOM* **2020**, 72, 4551.
- [27] M. Alfreider, R. Bodlos, L. Romaner, D. Kiener, *Acta Mater.* **2022**, 230, 117813.
- [28] B. Seligmann, Master Thesis, *Montanuniversität Leoben*, **2022**.
- [29] T. Walter, G. Khatibi, M. Nelhiebel, W. Heinz, W. Robl, *Mater. Sci. Forum* **2015**, 825–826, 983.
- [30] P. Hoffmann, S. Moser, C. Kofler, M. Nelhiebel, D. Tscharnuter, B. Karunamurthy, H. E. Pettermann, M. Todt, *Int. J. Fatigue* **2022**, 155, 106627.
- [31] R. Schöngundner, R. Treml, T. Antretter, D. Kozic, W. Ecker, D. Kiener, R. Brunner, *Thin Solid Films* **2014**, 564, 321.
- [32] R. Treml, D. Kozic, J. Zechner, X. Maeder, B. Sartory, H. P. Ganser, R. Schöngundner, J. Michler, R. Brunner, D. Kiener, *Acta Mater.* **2016**, 103, 616.
- [33] I. Noyan, J. Cohen, *Residual Stress: Measurement By Diffraction and Interpretation*, Springer, Berlin, Germany **1987**.
- [34] V. Hauk, *Structural and Residual Stress Analysis by Nondestructive Methods: Evaluation-Application-Assessment*, Elsevier Science B. V., Amsterdam, The Netherlands **1997**.
- [35] R. Venkatraman, J. C. Bravman, W. D. Nix, P. W. Avies, P. A. Flinn, D. B. Fraser, *J. Electron. Mater.* **1990**, 19, 1231.
- [36] G. G. Stoney, C. A. Parsons, *Proc. R. Soc. London Ser. A* **1909**, 82, 172.
- [37] A. M. Korsunsky, M. Sebastiani, E. Bemporad, *Surf. Coat. Technol.* **2010**, 205, 2393.
- [38] X. Song, K. B. Yeap, J. Zhu, J. Belnoue, M. Sebastiani, E. Bemporad, K. Zeng, A. M. Korsunsky, *Thin Solid Films* **2012**, 520, 2073.
- [39] M. J. Pfeifenberger, M. Mangang, S. Wurster, J. Reiser, A. Hohenwarter, W. Pfleging, D. Kiener, R. Pippan, *Mater. Des.* **2017**, 121, 109.
- [40] D. Kiener, C. Motz, M. Rester, M. Jenko, G. Dehm, *Mater. Sci. Eng. A* **2007**, 459, 262.
- [41] R. Fritz, D. Kiener, *Measurement* **2017**, 110, 356.
- [42] J. Canny, *IEEE Trans. Pattern Anal. Mach. Intell.* **1986**, 6, 679.
- [43] S. Timoshenko, *J. Opt. Soc. Am.* **1925**, 11, 233.
- [44] G. Dehm, T. J. Balk, H. Edongué, E. Arzt, *Microelectron. Eng.* **2003**, 70, 412.
- [45] T. J. Balk, G. Dehm, E. Arzt, *Acta Mater.* **2003**, 51, 4471.
- [46] M. A. Meyers, K. K. Chawla, *Mechanical Behavior of Materials*, Cambridge University Press, Cambridge UK **2008**.
- [47] G. Gottstein, *Materialwissenschaft Und Werkstofftechnik*, Springer Vieweg Berlin, Heidelberg Germany **2014**.
- [48] S. Chen, Y. F. En, G. Y. Li, Z. Z. Wang, R. Gao, R. Ma, L. X. Zhang, Y. Huang, *Microelectron. Reliab.* **2020**, 112, 113826.
- [49] S. Massl, H. Köstenbauer, J. Keckes, R. Pippan, *Thin Solid Films* **2008**, 516, 8655.
- [50] A. M. Korsunsky, M. Sebastiani, E. Bemporad, *Mater. Lett.* **2009**, 63, 1961.
- [51] E. Bemporad, M. Brisotto, L. E. Epero, M. Gelfi, A. M. Korsunsky, A. J. G. Lunt, *Thin Solid Films* **2014**, 572, 224.
- [52] S. Adachi, *Properties of Semiconductor Alloys: Group-IV, III-V and II-VI Semiconductors*, John Wiley & Sons, Hoboken **2009**.
- [53] G. Kirchgaßner, Bachelor Thesis, *Montanuniversität Leoben*, **2020**.
- [54] Engineers Edge, Poisson's Ratio Metals Materials Chart, https://www.engineersedge.com/materials/poissons_ratio_metals_materials_chart_13160.htm, (accessed: August 2022).
- [55] S. Berger, O. Raslin, *Thin Solid Films* **1998**, 333, 264.
- [56] Matweb, Copper, Cu; Annealed, <https://www.matweb.com/search/datasheet.aspx?matguid=9aeb83845c04c1db5126fada6f76f7e>, (accessed: August 2022).
- [57] K.-H. Grote, J. Feldhusen, *Dubbel*, Springer, Berlin, Germany **2014**.
- [58] J. Dolbow, M. Gosz, *Mech. Mater.* **1996**, 23, 311.
- [59] P. Hess, *Appl. Surf. Sci.* **1996**, 106, 429.